



# Atomically dispersed cerium sites in carbon-doped boron nitride for photodriven CO<sub>2</sub> reduction: Local polarization and mechanism insight

Jingkuo Guo<sup>a</sup>, Yandong Duan<sup>a,\*</sup>, Tianjiao Wu<sup>a</sup>, Wanyu Zhang<sup>a</sup>, Lin Wang<sup>a</sup>, Yumei Zhang<sup>a</sup>, Qingzhi Luo<sup>a</sup>, Qiong Lu<sup>a</sup>, Yaqiang Zhang<sup>a</sup>, Huiying Mu<sup>a</sup>, Huaiyu Zhang<sup>b</sup>, Qiqi Han<sup>c</sup>, Desong Wang<sup>a,d,\*\*</sup>

<sup>a</sup> Hebei Key Laboratory of Photoelectric Control on Surface and Interface, School of Sciences, Hebei University of Science and Technology, Shijiazhuang 050018, People's Republic of China

<sup>b</sup> Institute of Computational Quantum Chemistry, College of Chemistry and Materials Science, Hebei Normal University, Shijiazhuang 050024, People's Republic of China

<sup>c</sup> Shanxi Supercomputing Center, Lvliang, Shanxi Province 033000, People's Republic of China

<sup>d</sup> State Key Laboratory of Metastable Materials Science and Technology (MMST), Hebei Key Laboratory of Applied Chemistry, Yanshan University, Qinhuangdao 066004, People's Republic of China

## ARTICLE INFO

### Keywords:

Cerium single atom  
Photocatalytic CO<sub>2</sub> reduction  
Selectivity  
Local polarization  
Carbon-doped BN

## ABSTRACT

The rapid recombination of photogenerated electrons and holes on the bulk and surface of photocatalyst and the limited active sites seriously hinder the photocatalytic efficiency. Herein, we present a single-atom local coordination strategy to solve the above problems of C-BN photocatalysts. By introducing Ce atoms to form the Ce/B<sub>2</sub>N<sub>2</sub> local structure, on the one hand, can effectively induce local polarization and form a local polarized electric field, which can promote the separation of photogenerated carriers. On the other hand, new Ce active sites are introduced and show a lower energy barrier for dissociation of the critical intermediate COOH\*, while suppressing CH<sub>4</sub> and H<sub>2</sub> evolution in the competing reaction. The Ce/C-BN delivers a selective CO formation rate of 125.5 μmol g<sup>-1</sup> h<sup>-1</sup> in pure water and is one of the best photocatalysts in the system without additives. This work offers valuable guidance for the rational design of efficient photocatalysts.

## 1. Introduction

Fossil fuel, ecological imbalance, and energy shortage seriously threaten the sustainable development of society. Converting CO<sub>2</sub> into high value-added chemicals by photocatalytic technology can produce renewable energy, and mitigate the greenhouse effect [1–4]. Due to the high chemical stability of CO<sub>2</sub> and the diversity of products, the CO<sub>2</sub> reduction reaction is a complicated problem. It is still a challenge to develop a cost-effective photocatalytic CO<sub>2</sub> reduction (PCR) catalyst with high efficiency and selectivity [5–8].

The concept of single-atom catalysts (SACs) has emerged as a new frontier of catalysis science in recent years due to their maximum atom utilization efficiency, high activity, and selectivity. SACs also have uniformly distributed undercoordinated active sites, providing a model system for bridging the gap between heterogeneous and homogeneous catalysis [9–15]. The catalytic performance of a single metal atom can

be significantly regulated by adjusting coordination anions (usually C, N, O, S, P), thus changing the local electronic structure of the active center. SACs generally exhibit catalytic properties different from their nanoscale metal counterparts [13,16,17]. At present, rare earth elements are widely used in the field of catalysis because of their rich electronic energy levels, known as "industrial vitamins". The abundant electron orbitals of rare earth elements can form strong coordination bonds with anions on the support, thus endowing them with different catalytic properties [18–21]. Li et al. synthesized rare single erbium atom supported on carbon nitride nanotubes for the efficient and stable photocatalytic performance of CO<sub>2</sub> reduction reaction [22]. Dong et al. designed and prepared La single atoms on carbon nitride (O/La-CN). The La single atom is anchored between the g-C<sub>3</sub>N<sub>4</sub> layers to form a single-atom La-N charge bridge. The O/La-CN has high selective photocatalytic reduction performance, and the CO generation rate reaches 92 μmol g<sup>-1</sup> h<sup>-1</sup> [23]. Cerium is the most abundant rare earth element,

\* Corresponding author.

\*\* Corresponding author at: Hebei Key Laboratory of Photoelectric Control on Surface and Interface, School of Sciences, Hebei University of Science and Technology, Shijiazhuang 050018, People's Republic of China.

E-mail addresses: [ydduan@iccas.ac.cn](mailto:ydduan@iccas.ac.cn) (Y. Duan), [dswang06@126.com](mailto:dswang06@126.com) (D. Wang).

<https://doi.org/10.1016/j.apcatb.2022.122235>

Received 24 September 2022; Received in revised form 11 November 2022; Accepted 27 November 2022

Available online 28 November 2022

0926-3373/© 2022 Elsevier B.V. All rights reserved.

and cerium compounds have attracted much attention due to their intriguing properties under irradiation. Cerium-based materials can hop between Ce (III) and Ce (IV) valence states, making them useful for reactant activation in heterogeneous catalysis [24,25]. When Ce species are decreased from nanoscale to single atomic level, the catalytic activity is further improved due to the greatly enhanced surface free energy [26,27]. However, the preparation of Ce monoatomic photocatalysts is still a great challenge, and the related mechanism has not been reported.

Hexagonal boron nitride (h-BN), as a two-dimensional (2D) material, was mainly considered inert material and used commercially as an insulator due to its poor electrical conductivity. In recent years, due to its distinguished properties, h-BN has attracted much attention in green energy, especially in catalysis [28–31]. The wide band gap limits its application in the field of photocatalysis, and it has been reported that the band structure of BN can be adjusted by doping C atoms, which can be used in the field of photocatalysis [32–37].

In this work, Ce/C-BN catalyst was prepared by introducing Ce atom into C-BN support. Ce/C-BN exhibits high selective photocatalytic reduction performance with the CO generation rate of  $125.5 \mu\text{mol g}^{-1} \text{h}^{-1}$ . It is found that the introduction of Ce leads to the local polarization of the structure, resulting in the formation of a local electric field, which promotes charge separation. This strategy provides a new opportunity to improve the photocatalytic performance of C-BN, which may stimulate further study of coordination engineering for single-atom catalysts.

## 2. Experimental section

### 2.1. Materials

D-(+)-Glucose ( $\text{C}_6\text{H}_{12}\text{O}_6$ ), Melamine ( $\text{C}_3\text{H}_6\text{N}_6$ ), Boric acid ( $\text{H}_3\text{BO}_3$ ), and Cerium nitrate hexahydrate ( $\text{Ce}(\text{NO}_3)_3 \cdot 6 \text{H}_2\text{O}$ ) were purchased from Shanghai Aladdin Biochemical Technology Co., LTD (Shanghai, China). Deionized water was used for the synthesis and testing process.

### 2.2. Preparation of C-BN and Ce/C-BN

Firstly,  $\text{Ce}(\text{NO}_3)_3 \cdot 6 \text{H}_2\text{O}$  (0.3458 g) was added to the deionized water (800 mL) under vigorous stirring. Next, a certain amount of glucose (13.50 g) and melamine (18.92 g) were added to the above solution under stirring at  $98^\circ\text{C}$ . After glucose and melamine were dissolved,  $\text{H}_3\text{BO}_3$  (27.82 g) was added to the mixture, and then the mixture was stirred at  $90^\circ\text{C}$  for 6 h. After the suspension was cooled to room temperature, it was filtered and dried in vacuum at  $60^\circ\text{C}$  for 48 h. The dried sample was loaded in a furnace and heated up to  $900^\circ\text{C}$  for 12 h in  $\text{N}_2$  atmosphere, and the Ce/C-BN was obtained. The C-BN was prepared with the same synthesis procedure of Ce/C-BN except that  $\text{Ce}(\text{NO}_3)_3 \cdot 6 \text{H}_2\text{O}$  was not added.

### 2.3. Characterization

The morphology of the catalysts was observed by transmission electron microscopy (TEM, JEM-F200), scanning electron microscopy (SEM, Czech Republic TESCAN MIRA LMS), and aberration-corrected transmission electron microscopy (AC-TEM, JEM-ARM300F). X-ray diffraction (XRD) patterns were collected on a powder diffractometer (D/max 2500PC, Rigaku), using  $\text{Cu-K}\alpha$  radiation as X-ray source ( $\lambda = 0.15406 \text{ nm}$ , 40 kV, 150 mA) in the scanning range of  $20\text{--}80^\circ$  ( $2\theta$ ). The Brunauer-Emmett-Teller (BET) surface area and pore size distribution of the catalysts by nitrogen adsorption-desorption experiment using TriStar II 3020. Prior to analysis, the prepared catalyst was degassed at  $200^\circ\text{C}$  for 10 h to remove the adsorbed water and other impurities on the surface. X-ray photoelectron spectroscopy (XPS) was performed on a Thermo Scientific K-Alpha instrument with 72 W Al  $\text{K}\alpha$  X-rays as the excitation source. The binding energies were calibrated by contaminant C at 284.8 eV. The light absorption of the photocatalyst was determined

by Ultraviolet-visible (UV-vis) diffuse reflectance spectra (DRS, UV-2550). The photoluminescence (PL) spectrum was obtained on F-4600 (Tokyo Japan) under 260 nm laser irradiation. Fourier transform infrared (FT-IR) spectra were performed on a Thermo-Fisher scientific Prestige-21 FT-IR instrument using KBr as dilute agent. In situ FT-IR measurements were conducted using the Bruker INVENIOR FT-IR spectrometer equipped with an in situ diffuse reflectance cell (Harrick). In-situ FT-IR measurements were performed to explore the activation process and intermediates of the  $\text{CO}_2$  photoreduction process occurring on C-BN and Ce/C-BN under dark and irradiation conditions. The Ce concentrations in the samples were analyzed by inductively coupled plasma mass spectrometry (ICP-MS, Agilent 7800). Ce  $L_{3\text{-edge}}$  analysis was conducted in transmission mode on beamline 12-BM in the Advanced Photon Source at Argonne National Laboratory. Before the analysis at the beamline, samples were pressed into thin sheets with 1 cm in diameter and sealed using tape film. Ce  $L_{3\text{-edge}}$  extended X-ray absorption fine structure (EXAFS), and X-ray absorption near-edge structure (XANES) spectra were recorded in transmission mode. XANES and EXAFS data reduction and analysis were analyzed by Athena and Artemis software.

### 2.4. Photocatalytic activity and electrochemical measurement

In a typical activity test, 0.05 g of the catalyst was dispersed in a certain amount of water, and then the reactor was purged with  $\text{CO}_2$  gas in the dark for 30 min. The reactor was irradiated by a 300 W Xe lamp (PLS-SXE300, AM 1.5 G, Beijing Perfectlight). The products ( $\text{CO}$ ,  $\text{H}_2$ , and  $\text{CH}_4$ ) concentrations were analyzed by GC9700 gas chromatography (Fili Instruments, China) equipped with a thermal conductivity detector (TCD) and flame ionization detector (FID) with  $\text{N}_2$  as the carrier gas. The isotope-labeled experiments ( $^{13}\text{CO}_2$ ) were performed on gas chromatography-mass spectrometry (GC-MS) (6980 N network GC system-5975 inert mass selective detector, Agilent Technologies, USA). The apparent quantum efficiency (AQE) for PCR was obtained with monochromatic light of 385, 400, 420, 450, and 500 nm, and calculated as follows:  $\text{AQE} = \frac{N_p}{N_p} \times 100\% = \frac{2 \times M \times N_A \times h \times c}{S \times P \times t \times \lambda} \times 100\%$ . Where  $N_p$  is the total incident photons,  $N_e$  is the total reaction electrons,  $M$  is the number of product molecules (mol),  $N_A$  is Avogadro constant,  $h$  is the Planck constant,  $c$  is the speed of light (m/s),  $S$  is the irradiation area ( $\text{cm}^2$ ),  $P$  is the intensity of irradiation light ( $\text{W cm}^{-2}$ ),  $t$  is the photoreaction time (s) and  $\lambda$  is the wavelength of the monochromatic light (m).

Electrochemical measurements were performed on a CHI 660E electrochemical workstation, using ITO glass, platinum wire, Ag/AgCl as working electrode, a counter electrode, and reference electrode respectively. Before the preparation of the working electrode, 10 mg powder sample was dispersed into 1 mL ultrapure water, and 50  $\mu\text{L}$  Nafion solution was added to form a uniform suspension by ultrasound for 30 min. Then, the suspension was coated on ITO glass and dried at room temperature. In the test, the interval of illumination is 20 s (light 20 s, dark 20 s). In addition, the electrolyte is aqueous 0.2 M  $\text{Na}_2\text{SO}_4$ , and the light source is a full spectrum xenon lamp light (300 W).

### 2.5. Theoretical calculation

DFT calculations were performed using the Vienna ab initio simulation packages with the projector-augmented wave (PAW) pseudopotentials [38–40], and PBE-GGA exchange-correlation functional was adopted [41]. A  $6 \times 6$  supercell was employed for C-BN and Ce/C-BN with a vacuum thickness of  $> 15 \text{ \AA}$ . The DFT+D3 method was employed to accurately describe the weak interactions [42,43]. The plane wave cutoff was set to 450 eV. Gamma centered k-point meshes of  $1 \times 1 \times 1$  were used for all calculations except that  $2 \times 2 \times 1$  for density of state (DOS). The Gibbs free energy changes ( $\Delta G$ ) were calculated to understand the reaction path for  $\text{CO}_2$  reduction.  $\Delta G$  is defined as  $\Delta G = \Delta E + \Delta E_{\text{ZPE}} - T\Delta S$ , where  $\Delta E$  is the change of reaction energy,  $\Delta E_{\text{ZPE}}$

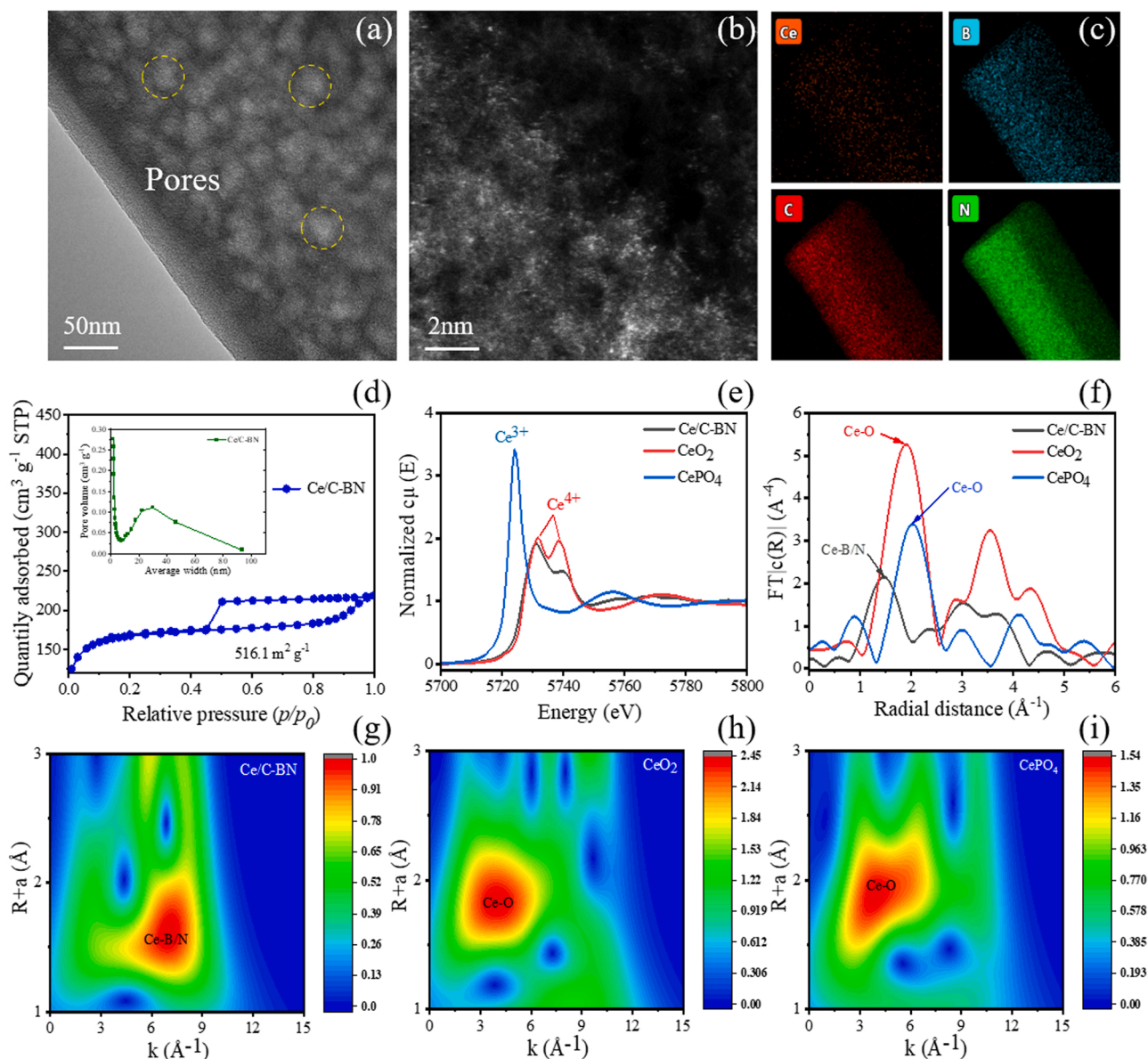


**Fig. 1.** (a) TEM image of Ce/C-BN. (b) AC-TEM image of Ce/C-BN. (c) EDS elemental maps of Ce/C-BN. (d) N<sub>2</sub> adsorption-desorption isotherms and the corresponding pore size distribution curve of Ce/C-BN. (e) X-ray absorption near-edge structure (XANES) of Ce/C-BN, CeO<sub>2</sub>, and CePO<sub>4</sub> at the Ce L<sub>3</sub>-edge. (f) Fourier-transformed extended X-ray absorption fine structure (FT-EXAFS) spectra of Ce/C-BN, CeO<sub>2</sub>, and CePO<sub>4</sub> at the Ce L<sub>3</sub>-edge. (g)-(i) Wavelet transform (WT) of Ce/C-BN, CeO<sub>2</sub>, and CePO<sub>4</sub>.

is the change of zero-point energy,  $T$  is the temperature (298.15 K), and  $\Delta S$  is the change in entropy.

### 3. Results and discussion

#### 3.1. Catalyst characterization

The C-BN and Ce/C-BN samples were first characterized by XRD (Fig. S1), and both samples show poor crystallinity. The three peaks of the C-BN and Ce/C-BN samples located at 23.5°, 42.6°, and 76.8° can be indexed as h-BN (002), (100), and (110) planes [44,45]. All peaks are broad and weak, indicating the defect-rich structures, and the results show that the introduction of Ce has no effect on the crystallinity. Scanning electron microscopy (SEM) was employed to investigate the morphology of the C-BN and Ce/C-BN samples (Fig. S2). The as-prepared C-BN and Ce/C-BN exhibits wrinkle surfaces with a large number of pores and outstanding edges, and these pores belong to

through-holes with diameters ranging from 20 to 50 nm (Fig. 1d), and the introduction of Ce atom has no obvious effect on the pore structure and specific surface area of C-BN (Fig. S3). The morphology of Ce/C-BN samples was further studied by TEM (Fig. 1a, S4), and the pores are labeled with yellow circles. The HRTEM image was enlarged to 2 nm, and no CeO<sub>2</sub> is observed in the image (Fig. S5). Abundant bright spots are observed by AC-TEM imaging (Fig. 1b), indicating that most of the Ce single atoms are uniformly distributed on the Ce/C-BN despite the presence of a small number of clusters. Additionally, the energy-dispersive X-ray (EDX) spectroscopy elemental mappings demonstrate the homogeneous dispersion of Ce, B,

C, and N atoms over the entire architectures (Fig. 1c, S6). X-ray absorption spectrum (XAS) was carried out to further understand the Ce configurations in Ce/C-BN. The typical L<sub>3</sub>-edge XANES features of Ce<sup>3+</sup> are distinctly different from those of Ce<sup>4+</sup> (Fig. 1e). Ce<sup>3+</sup> displays a strong single peak around 5724 eV, while Ce<sup>4+</sup> appears two well-separated maximum peaks of lower intensity around 5732 and



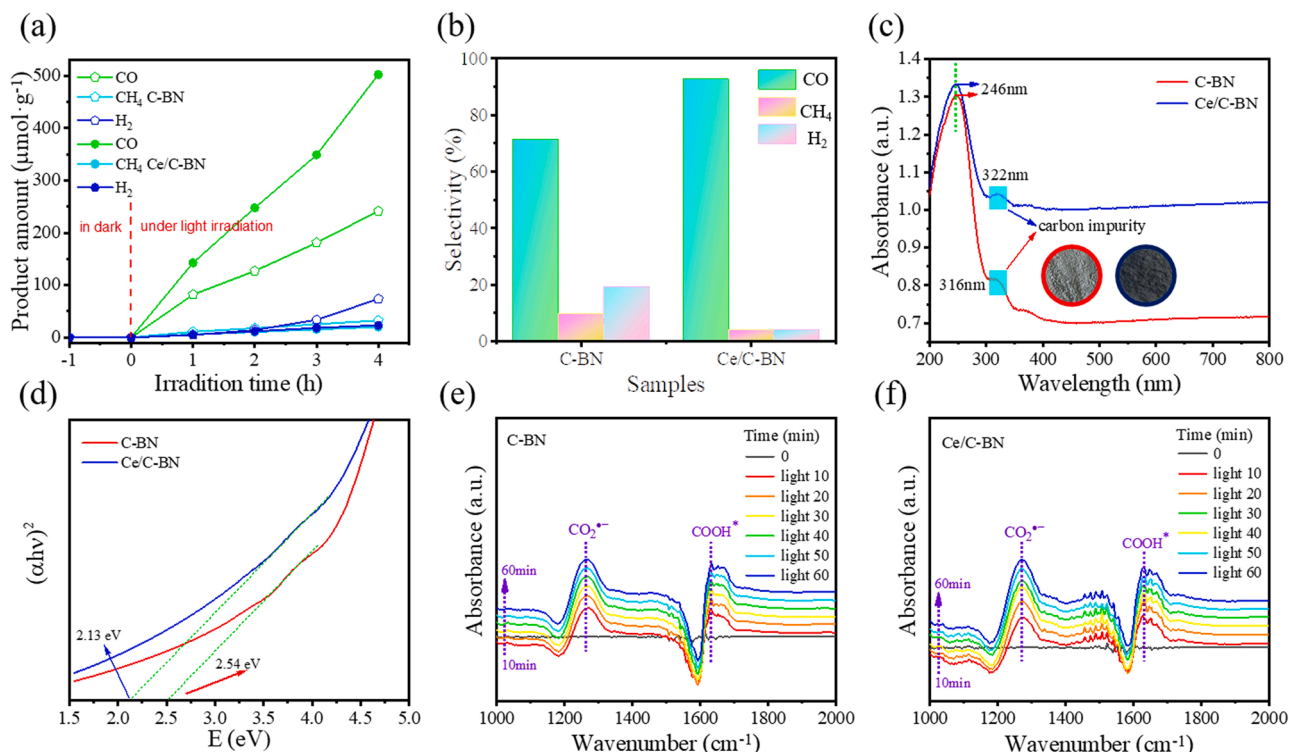


**Fig. 2.** (a) The photocatalytic CO<sub>2</sub> reduction performances of C-BN and Ce/C-BN samples. (b) The selectivity of CO, CH<sub>4</sub> and H<sub>2</sub> evolution on C-BN and Ce/C-BN samples. (c) UV-vis diffuse reflectance spectra of C-BN and Ce/C-BN. (d) Plots of (αhν)<sup>2</sup> versus E based on the optical absorption data from C-BN and Ce/C-BN samples, respectively. (e)-(f) In-situ FT-IR spectra of photocatalytic CO<sub>2</sub> reduction on C-BN and Ce/C-BN.

5738 eV. The Ce L<sub>3</sub>-edge XANES spectrum of Ce/C-BN shows that the maximum peak is similar to Ce<sup>4+</sup> at 5731 eV. The XANES spectra explicitly indicate that the oxidation of Ce in Ce/C-BN is ionic Ce<sup>4+</sup>, and this result is consistent with the XPS spectra (Fig. S7) [46]. The Fourier-transformed (FT) extended X-ray absorption fine structure (EXAFS) analysis of Ce/C-BN reveals that there is a broader peak at 1.47 Å lower than that of Ce-O scattering (1.90 Å) in CeO<sub>2</sub> and the Ce-O scattering (2.02 Å) in CePO<sub>4</sub>. This broader peak can be defined as Ce-B/N, due to the high coordination number of single Ce atoms, which can be stabilized by N and B in C-BN matrix. Furthermore, the absence of Ce-Ce paths at 3.56 Å clearly indicates the atomic dispersion of Ce atoms in Ce/C-BN. The coordination numbers of Ce-B and Ce-N within Ce/C-BN are 2, according to the fitting parameters given in Table S1 and Fig. S8. To intensify these results, we performed a wavelet transform (WT) analysis (Fig. 1g-i). Compared with those of the CeO<sub>2</sub> and CePO<sub>4</sub>, WT plots of the Ce/C-BN exhibit only one intensity maximum at around 7 Å<sup>-1</sup>, which can be assigned to Ce-B/N coordination. This result suggests that the Ce atoms on Ce/C-BN exist as isolated Ce atoms without the presence of metallic Ce crystalline structures. Combined with the experimental results and XPS analysis in Fig. S9, we first determined the structure of C-BN (Fig. S10), and then constructed four structural models of Ce/C-BN, as shown in the Fig. S11. Compared with other structures, structure b has lower energy, so this structure is adopted in the subsequent DFT calculations.

### 3.2. Catalyst performance

The main product of CO<sub>2</sub> reduction of C-BN and Ce/C-BN samples under Xenon light irradiation is CO. As shown in Fig. 2a, the yields of CO, CH<sub>4</sub> and H<sub>2</sub> increase almost linearly with irradiation time. When the catalyst is C-BN, the total amount of CO, CH<sub>4</sub> and H<sub>2</sub> obtained in 4 h are 242, 33 and 74 μmol g<sup>-1</sup>, respectively, and the selectivity of CO, CH<sub>4</sub> and H<sub>2</sub> generation is 71.2 %, 9.6 % and 19.1 %, respectively (Fig. 2b). The CO, CH<sub>4</sub> and H<sub>2</sub> produced by Ce/C-BN within 4 h are 502, 20 and

23 μmol g<sup>-1</sup>, respectively, and the selectivity is 92.5 %, 3.7 % and 3.8 %. Based on the above results, Ce/C-BN catalyst can significantly improve the CO yield and inhibit the formation of CH<sub>4</sub> and H<sub>2</sub> under the same conditions. As a control experiment, we carried out the reaction in the dark or in an Ar atmosphere and found that none of the desired products was observed. The results show that CO and CH<sub>4</sub> are derived from the photoreduction of CO<sub>2</sub> rather than impurities in the reactor (Fig. 2a, Fig. S12). The <sup>13</sup>C isotope labeling experiment was further conducted to confirm the source of carbon in the products, and the results are shown in Fig. S13. The signals at m/z = 29 and 17 can be attributed to <sup>13</sup>CO and <sup>13</sup>CH<sub>4</sub>, indicating that the carbon source of the product is derived from the used CO<sub>2</sub>. In the photocatalytic stability experiment, the reactor was vacuumed and renewed with water without further treatment and subjected to next cycling run. The obtained photocatalytic activity was maintained for 5 cycles with a rate change of only within 3 % (Fig. S14), and no leaching of Ce was observed for the used Ce/C-BN after cycling runs (Table S2). Why does the C-BN sample exhibit such excellent properties after the introduction of Ce? We first analyzed the light absorption capacity of the two materials. The UV-Vis diffuse reflectance spectra (DRS) of C-BN and Ce/C-BN are shown in Fig. 2c. Compared with C-BN, the absorption edge of Ce/C-BN shifts to a longer wavelength, and the visible light response increases significantly. The introduction of cerium atom enhances the absorption of the visible spectrum, which is beneficial to improving photocatalytic performance. Both C-BN and Ce/C-BN have broad absorption peaks at 246 nm, which is the resonance exciton effect caused by π-π transition [47]. In addition, a new absorption peak at 316 nm of C-BN, and at 322 nm of Ce/C-BN is observed, which is related to the carbon impurities. As calculated by the Tauc plot method from the DRS spectra (Fig. 2d) [48], the Ce/C-BN corresponding to an optical band gap of 2.13 eV, which is more narrow than the C-BN absorption edge corresponds to an optical band gap of 2.54 eV. The narrowing of the band gap is attributed to the appearance of two isolated impurity levels just above and below the valence band with the introduction of Ce (Fig. S15). The wavelength dependence of the AQE was

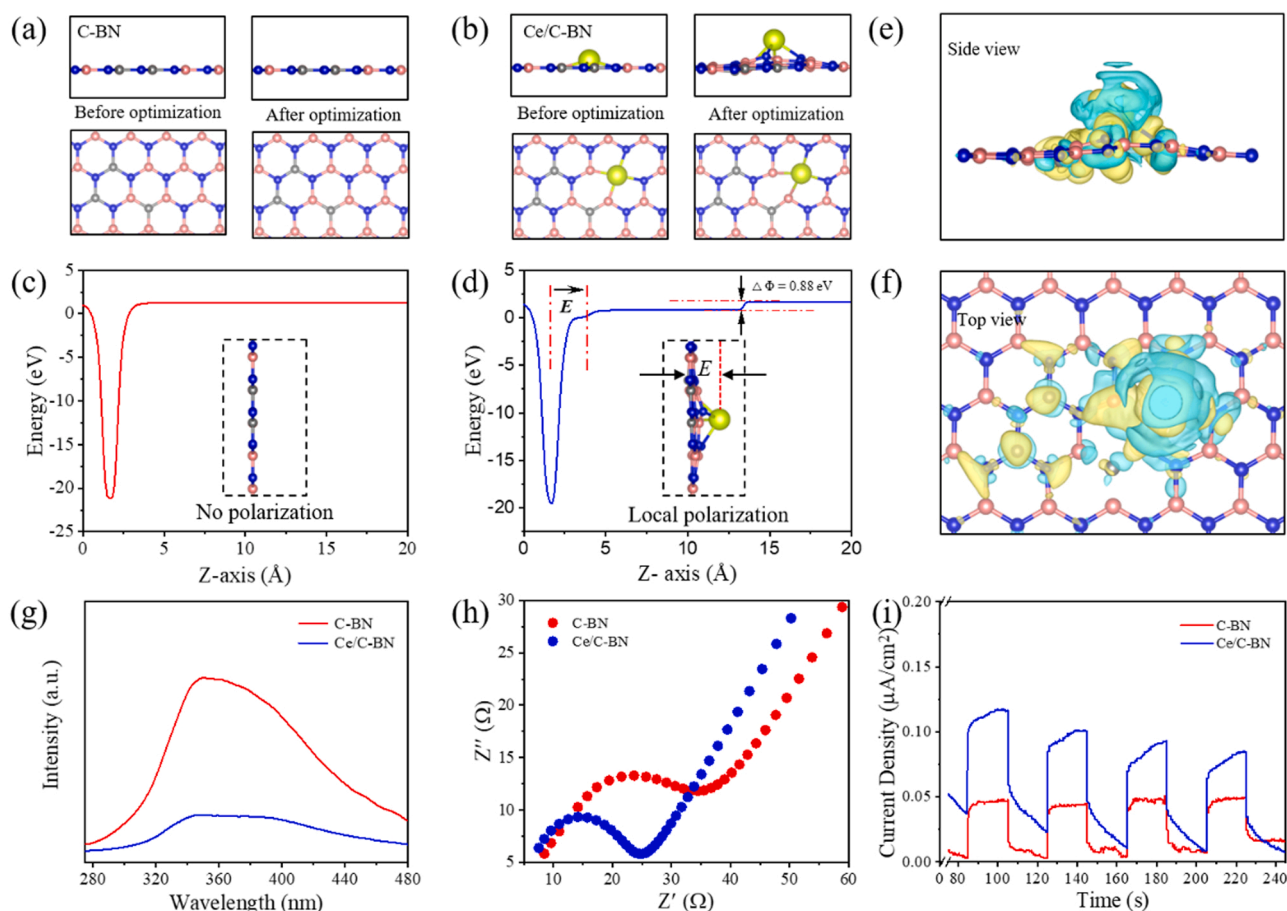


**Fig. 3.** (a) The atomic structure of C-BN before and after optimization. (b) The atomic structure of Ce/C-BN before and after optimization. The pink, blue, silver, and yellow spheres represent B, N, C, and Ce atoms, respectively. Planar average electrostatic potential energy of the (c) C-BN and (d) Ce/C-BN.  $\Delta\Phi$  is the potential energy difference. The differential charge density (yellow area refers to charge accumulation and blue area refers to charge loss) of Ce/C-BN: (e) side view and (f) top view. (g) Photoluminescence spectra of C-BN and Ce/C-BN. (h) EIS Nyquist plots of C-BN and Ce/C-BN. (i) Transient photocurrent density responses of C-BN and Ce/C-BN.

calculated for C-BN and Ce/C-BN (Fig. S16), and the results show that AQE is positively correlated with the light absorption capacity of the material. The in-situ FT-IR results of C-BN and Ce/C-BN are shown in Fig. 2e-f. Two distinct peaks are observed, and the intensity of each peak increases with the increase of irradiation time. The peaks at 1268 and 1630  $\text{cm}^{-1}$  are ascribed to the  $\text{CO}_2^*$  group and the  $\text{COOH}^*$  group, respectively [49,50]. These peaks are the primary intermediates of  $\text{CO}_2$  reduction process. At the same time, the peaks at 1540 and 1673  $\text{cm}^{-1}$  (Fig. S17-18) are attributed to monodentate carbonate ( $\text{m-CO}_3^*$ ). These carbonates are probably derived from the interaction between  $\text{CO}_2$  and water vapor. In addition, the peak at 1457  $\text{cm}^{-1}$  belongs to the methyl group, which further indicates the formation of product  $\text{CH}_4$  [51]. The peak attributed to methyl groups was more evident on Ce/C-BN rather than C-BN. This phenomenon may be attributed to the fact that the adsorption capacity of  $\text{CH}_4$  on Ce/C-BN is stronger than that on C-BN (Fig. S19). Although only a small amount of  $\text{CH}_4$  is generated, the  $\text{CH}_4$  adsorbed on the catalyst is more easily detected in the in-situ FT-IR.

### 3.3. The role of Ce in Ce/C-BN and catalytic mechanism

We then calculate the plane average potentials of C-BN and Ce/C-BN. Fig. 3a-b shows the structural model of C-BN and Ce/C-BN, and Fig. 3c-d shows the planar average potential results. Due to the destruction of the mirror symmetry, there is an

intrinsic dipole moment in Ce/C-BN [52–54], and the built-in electric field points from the C-BN plane to the protruding Ce atom and the

electrostatic potential difference ( $\Delta\Phi$ ) is 0.88 eV. At the same time, the space charge distribution results show that the charge distribution is highly uneven, in which the area around Ce atom is in a charge depletion state (blue), and most areas of C-BN opposite Ce atom are in a charge accumulation state (yellow) (Fig. 3e, f), which is quite different from that of C-BN (Fig. S20). The existence of built-in electric field is advantageous to the separation of photogenerated charge carriers. We studied the photogenerated carrier separation efficiency of the samples by photoluminescence (PL) spectroscopy. Compared with the prepared C-BN, Ce/C-BN exhibits significant steady-state PL quenching (Fig. 3g). Electrochemical impedance spectroscopy (EIS, Fig. 3h) shows that the charge transfer resistance ( $R_{\text{ct}}$ ) of Ce/C-BN catalyst is significantly lower than that of C-BN catalyst, which also indicates that Ce/C-BN has an ultra-fast charge transfer rate. The photocurrent density results in Fig. 3i further prove the high directional migration efficiency of photogenerated electrons in Ce/C-BN.

Based on the above experimental results, the Ce atom must play an essential role in the thermodynamics of PCR. Taking into account the sensitivity of the surface structure of the materials to photocatalytic reactions, more extensive DFT calculations were performed to reveal the relationship between the structure and properties of C-BN and Ce/C-BN at the molecular surface level (Fig. 4). We first analyzed the adsorption energy of  $\text{CO}_2$  and the active intermediate  $\text{COOH}$  at the catalytic sites of C-BN and Ce/C-BN and (Fig. S21-24). When the adsorption energy is greater than zero, it indicates that the intermediate  $\text{COOH}^*$  is not easy to form at this site. Based on this result, the catalytic site of C-BN is C-BN1,

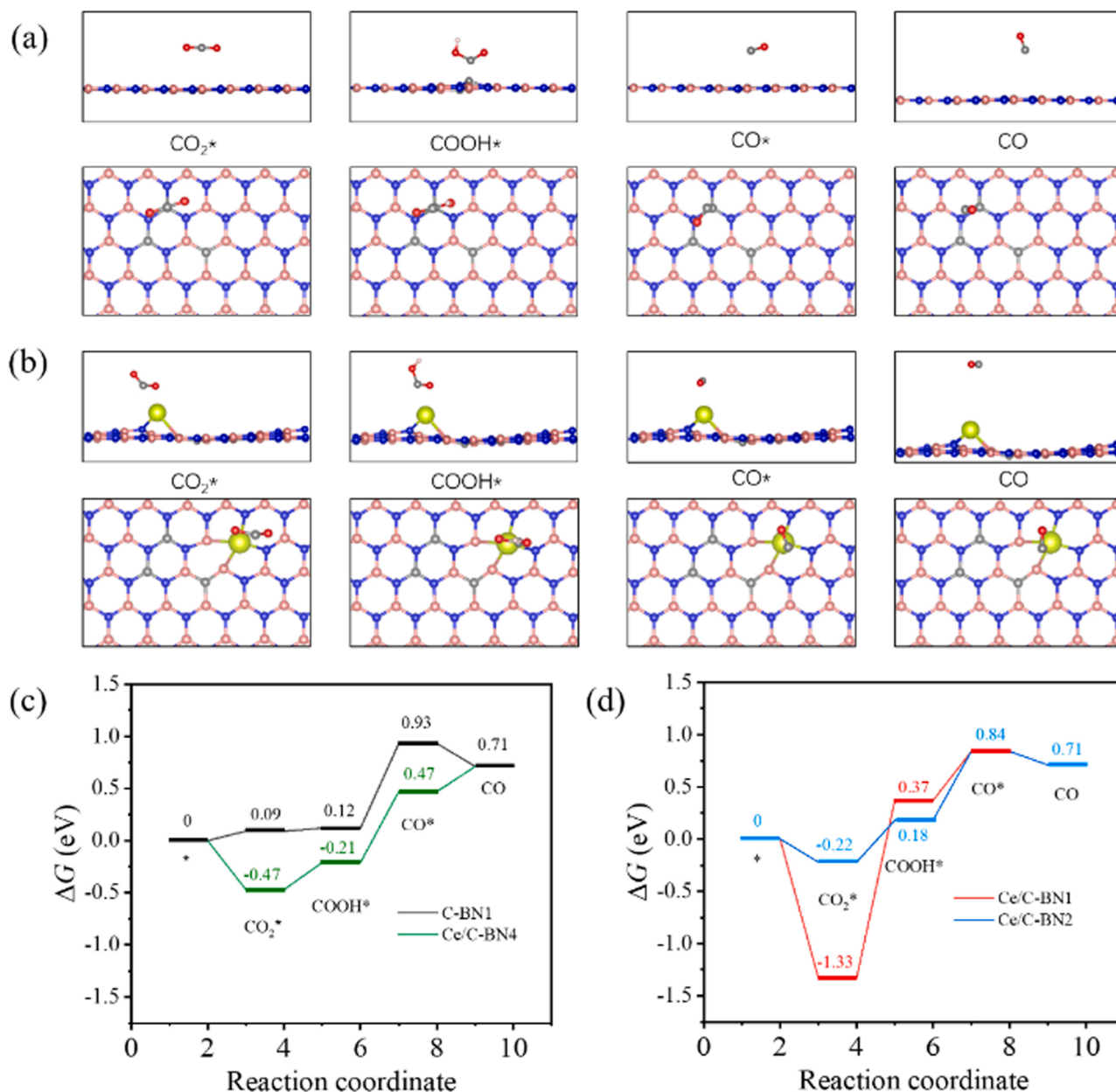


**Fig. 4.** DFT optimized structures of  $\text{CO}_2^*$ ,  $\text{COOH}^*$ ,  $\text{CO}^*$  and  $\text{CO}(\text{g})$  on (a) C-BN1 and (b) Ce/C-BN4. (c)-(d) Energy profile for the elementary steps of  $\text{CO}_2$  reduction to  $\text{CO}$  over C-BN and Ce/C-BN. “\*” indicates the surface adsorption state. The pink, blue, silver, yellow, red, and light pink spheres represent B, N, C, Ce, O, and H atoms, respectively.

and the possible catalytic sites of Ce/C-BN are Ce/C-BN1, Ce/C-BN2, and Ce/C-BN4. Furthermore, the conversion path from  $\text{CO}_2$  to  $\text{CO}$  was analyzed by DFT calculation (Fig. 4, S25). The rate-limiting step of the reaction at Ce/C-BN1 site is  $\text{COOH}^*$  formation. At the C-BN1, Ce/C-BN2, and Ce/C-BN4 sites, the decomposition of  $\text{COOH}^*$ , an intermediate generated by proton-coupled electron transfer, into  $\text{CO}$  and  $\text{OH}$  is a rate-limiting step because it has the highest energy barrier (Fig. 4c, d). The decomposition energy barrier of  $\text{COOH}^*$  at the three sites is 0.81 eV, 0.66 eV and 0.68 eV, respectively. Therefore, the introduction of Ce is beneficial to the formation of  $\text{CO}^*$ . For the Ce/C-BN4 site, the conversion of adsorbed  $\text{CO}^*$  to  $\text{CO}(\text{g})$  is a thermodynamically non-spontaneous process. Thus, for Ce/C-BN catalyst,  $\text{CO}$  is mainly produced from the Ce/C-BN2 site. As mentioned above, the  $\text{CO}$  selectivity of C-BN in the photocatalytic reduction of  $\text{CO}_2$  increases from 71.2 % to 92.5 %, and the side reactions of  $\text{CH}_4$  and  $\text{H}_2$  are significantly inhibited. The influence of surface molecular structure on selectivity was further analyzed.

Hydrogenation of adsorbed  $\text{CO}^*$  species to  $\text{CHO}^*$  is a key step in  $\text{CH}_4$  evolution [22,55,56]. It can be seen from Fig. 5b that the formation of  $\text{CHO}^*$  is spontaneous at all catalytic sites. The nudged elastic band method (NEB) was utilized for the transition state search between  $\text{CO}^*$  and  $\text{CHO}^*$  states. Notably, all sites on Ce/C-BN exhibit higher activation barriers than C-BN1 site (0.54 eV) (Fig. 5b). Therefore, the introduction of Ce is not conducive to the production of  $\text{CH}_4$ . Similarly, it can be seen from Fig. 5c, S26–27, the catalyst Ce/C-BN exhibits a significantly higher formation energy barrier of  $\text{H}_2$ . Thus, the  $\text{H}_2$  generation selectivity of the catalyst is also significantly inhibited after the introduction of Ce.

#### 4. Conclusion

In summary, we propose a novel local polarization strategy by introducing Ce single atoms, which greatly improves the photocatalytic

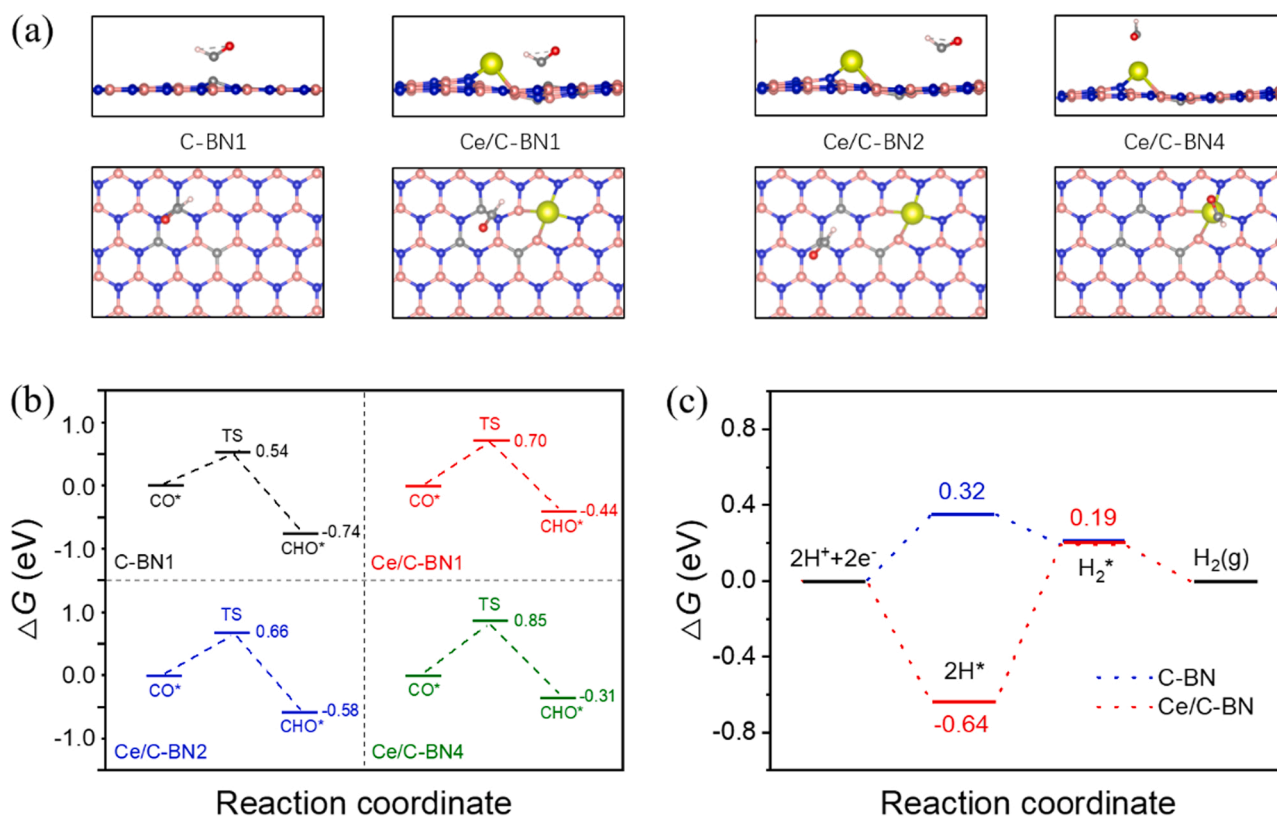


**Fig. 5.** (a) DFT optimized structures of CHO\* on different sites. (b) Energy barrier of CO\* to CHO\* on different sites. The pink, blue, silver, yellow, red, and light pink spheres represent B, N, C, Ce, O and H atoms, respectively. (c) Energy profile for the elementary steps of H<sub>2</sub>O reduction to H<sub>2</sub> over C-BN and Ce/C-BN. TS symbolizes transition states.

CO<sub>2</sub> reduction performance. Benefiting from the local polarization effect and the introduced isolated single-atom Ce active sites, the Ce/C-BN exhibits considerable photocatalytic activity for selective CO<sub>2</sub> reduction, yielding an impressive CO generation rate of 125.5  $\mu\text{mol g}^{-1} \text{h}^{-1}$ . Density functional theory analysis suggests that the introducing Ce changes the energy barrier of the thermodynamic rate determination step, thus significantly improving the catalytic activity and selectivity compared to the C-BN. This study deepens our understanding of charge separation in photocatalysis and provides a new strategy for rationally designing efficient photocatalysts.

#### CRediT authorship contribution statement

**Jingkuo Guo:** Data curation, Formal analysis, Investigation, Methodology, Writing - original draft. **Yandong Duan:** Conceptualization, Formal analysis, Funding acquisition, Methodology, Resources, Supervision, Writing - original draft, Writing - review & editing. **Tianjiao Wu:** Data curation. **Wanyu Zhang:** Data curation, Formal analysis. **Lin Wang:** Formal analysis. **Yumei Zhang:** Formal analysis. **Qingzhi Luo:** Investigation, Resources. **Qiong Lu:** Methodology. **Yaqiang Zhang:** Data curation, Methodology. **Huiying Mu:** Software. **Huaiyu Zhang:** Funding acquisition, Software. **Qiqi Han:** Resources. **Desong Wang:** Conceptualization, Formal analysis, Resources, Supervision.

#### Declaration of Competing Interest

The authors declare that they have no known competing financial interests or personal relationships that could have appeared to influence the work reported in this paper.

#### Data availability

No data was used for the research described in the article.

#### Acknowledgments

This work was supported by the Science and Technology Project of Hebei Education Department (ZD2022122), National Natural Science Foundation of China (No. 21903020) and the Natural Science Foundation of Hebei Province (No. B2021208007). The theoretical work was carried out at Shanxi Supercomputing Center of China, and the calculations were performed on TianHe-2. The authors would like to thank Manxiu Nie from shiyanjia Lab ([www.shiyanjia.com](http://www.shiyanjia.com)) for the specific surface area and pore structure analysis.

#### Appendix A. Supporting information

Supplementary data associated with this article can be found in the online version at [doi:10.1016/j.apcatb.2022.122235](https://doi.org/10.1016/j.apcatb.2022.122235).

#### References

- [1] F. Marques Mota, D.H. Kim, Chem. Soc. Rev. 48 (2019) 205–259.
- [2] K. Li, B. Peng, T. Peng, ACS Catal. 6 (2016) 7485–7527.
- [3] J. Albero, Y. Peng, H. García, ACS Catal. 10 (2020) 5734–5749.
- [4] N. Li, B. Wang, Y. Si, F. Xue, J. Zhou, Y. Lu, M. Liu, ACS Catal. 9 (2019) 5590–5602.
- [5] H. Huang, H. Song, J. Kou, C. Lu, J. Ye, J. Energy Chem. 67 (2021) 309–341.
- [6] J. Kou, C. Lu, J. Wang, Y. Chen, Z. Xu, R.S. Varma, Chem. Rev. 117 (2017) 1445–1514.
- [7] Z. Kovacic, B. Likozar, M. Huš, ACS Catal. 10 (2020) 14984–15007.
- [8] A.M. Bahmanpour, M. Signorile, O. Kröcher, Appl. Catal. B: Environ. 295 (2021) 120319.
- [9] X. Wei, X. Luo, N. Wu, W. Gu, Y. Lin, C. Zhu, Nano Energy 84 (2021), 105817.



- [10] Y. Wang, H. Su, Y. He, L. Li, S. Zhu, H. Shen, P. Xie, X. Fu, G. Zhou, C. Feng, D. Zhao, F. Xiao, X. Zhu, Y. Zeng, M. Shao, S. Chen, G. Wu, J. Zeng, C. Wang, *Chem. Rev.* 120 (2020) 12217–12314.
- [11] B. Singh, M.B. Gawande, A.D. Kute, R.S. Varma, P. Fornasiero, P. McNeice, R. V. Jagadeesh, M. Beller, R. Zboril, *Chem. Rev.* 121 (2021) 13620–13697.
- [12] R. Qin, K. Liu, Q. Wu, N. Zheng, *Chem. Rev.* 120 (2020) 11810–11899.
- [13] Z. Li, S. Ji, Y. Liu, X. Cao, S. Tian, Y. Chen, Z. Niu, Y. Li, *Chem. Rev.* 120 (2020) 623–682.
- [14] C. Gao, J. Low, R. Long, T. Kong, J. Zhu, Y. Xiong, *Chem. Rev.* 120 (2020) 12175–12216.
- [15] Y. Lu, Z. Zhang, H. Wang, Y. Wang, *Appl. Catal. B: Environ.* 292 (2021), 120162.
- [16] H. Cao, J. Wang, J.-H. Kim, Z. Guo, J. Xiao, J. Yang, J. Chang, Y. Shi, Y. Xie, *Appl. Catal. B: Environ.* 296 (2021), 120362.
- [17] W. Zhu, J. Fu, J. Liu, Y. Chen, X. Li, K. Huang, Y. Cai, Y. He, Y. Zhou, D. Su, J.-J. Zhu, Y. Lin, *Appl. Catal. B: Environ.* 264 (2020), 118502.
- [18] B. Zheng, J. Fan, B. Chen, X. Qin, J. Wang, F. Wang, R. Deng, X. Liu, *Chem. Rev.* 122 (2022) 5519–5603.
- [19] X. Shi, B. Cao, J. Liu, J. Zhang, Y. Du, *Small* 17 (2021), 2005371.
- [20] S. Zhang, S.E. Saji, Z. Yin, H. Zhang, Y. Du, C.H. Yan, *Adv. Mater.* 33 (2021), 2005988.
- [21] K. Seth, *Org. Chem. Front.* 9 (2022) 3102–3141.
- [22] S. Ji, Y. Qu, T. Wang, Y. Chen, G. Wang, X. Li, J. Dong, Q. Chen, W. Zhang, Z. Zhang, S. Liang, R. Yu, Yu Wang, D. Wang, Y. Li, *Angew. Chem. Int. Ed.* 59 (2020) 10651–10657.
- [23] P. Chen, B. Lei, X.A. Dong, H. Wang, J.P. Sheng, W. Cui, J.Y. Li, Y.J. Sun, Z. M. Wang, F. Dong, *ACS Nano* 14 (2020) 15841–15852.
- [24] W. Li, L. Jin, F. Gao, H. Wan, Y. Pu, X. Wei, C. Chen, W. Zou, C. Zhu, L. Dong, *Appl. Catal. B: Environ.* 294 (2021), 120257.
- [25] F. He, H. Li, Y. Ding, K. Li, Y. Wang, Z. Wu, *Carbon* 130 (2018) 636–644.
- [26] M. Zhu, C. Zhao, X. Liu, X. Wang, F. Zhou, J. Wang, Y. Hu, Y. Zhao, T. Yao, L. M. Yang, Y. Wu, *ACS Catal.* 11 (2021) 3923–3929.
- [27] J.C. Li, X. Qin, F. Xiao, C. Liang, M. Xu, Y. Meng, E. Sarnello, L. Fang, T. Li, S. Ding, Z. Lyu, S. Zhu, X. Pan, P.-X. Hou, C. Liu, Y. Lin, M. Shao, *Nano Lett.* 21 (2021) 4508–4515.
- [28] M. Rafiq, X. Hu, Z. Ye, A. Qayum, H. Xia, L. Hu, F. Lu, P.K. Chu, *Nano Energy* 91 (2022), 106661.
- [29] R. Han, F. Liu, X. Wang, M. Huang, W. Li, Y. Yamauchi, X. Sun, Z. Huang, *J. Mater. Chem. A* 8 (2020) 14384–14399.
- [30] K. Bu, J. Deng, X. Zhang, S. Kuboon, T. Yan, H. Li, L. Shi, D. Zhang, *Appl. Catal. B: Environ.* 267 (2020), 118692.
- [31] J. Deng, K. Bu, Y. Shen, X. Zhang, J. Zhang, K. Faungnawakij, D. Zhang, *Appl. Catal. B: Environ.* 302 (2022), 120859.
- [32] C. Huang, C. Chen, M. Zhang, L. Lin, X. Ye, S. Lin, M. Antonietti, X. Wang, *Nat. Commun.* 6 (2015) 7698.
- [33] X. Li, B. Lin, H. Li, Q. Yu, Y. Ge, X. Jin, X. Liu, Y. Zhou, J. Xiao, *Appl. Catal. B: Environ.* 239 (2018) 254–259.
- [34] L. Chen, M. Zhou, Z. Luo, M. Wakeel, A.M. Asiri, X. Wang, *Appl. Catal. B: Environ.* 241 (2019) 246–255.
- [35] M. Zheng, J. Shi, T. Yuan, X.J.A.C. Wang, *Angew. Chem. Int. Ed.* 130 (2018) 5585–5589.
- [36] Q. Lu, J. An, Y. Duan, Q. Luo, Y. Shang, Q. Liu, Y. Tang, J. Huang, C. Tang, R. Yin, D. Wang, *Catalysts* 12 (2022) 555.
- [37] W. Qu, P. Wang, M. Gao, J.Y. Hasegawa, Z. Shen, Q. Wang, R. Li, D. Zhang, *Environ. Sci. Technol.* 54 (2020) 9693–9701.
- [38] G. Kresse, D. Joubert, *Phys. Rev. B* 59 (1999) 1758–1775.
- [39] G. Kresse, J.J.Cms Furthmüller, *Comp. Mater. Sci.* 6 (1996) 15–50.
- [40] G. Kresse, J. Furthmüller, *Phys. Rev. B* 54 (1996) 11169–11186.
- [41] J.P. Perdew, K. Burke, M. Ernzerhof, *Phys. Rev. Lett.* 77 (1996) 3865–3868.
- [42] S. Grimme, S. Ehrlich, L. Goerigk, *J. Comb. Chem.* 32 (2011) 1456–1465.
- [43] S. Grimme, J. Antony, S. Ehrlich, H. Krieg, *J. Chem. Phys.* 132 (2010), 154104.
- [44] A. Kumar, G. Malik, S. Sharma, R. Chandra, R.S. Mulik, *Ceram. Int.* 47 (2021) 30985–30992.
- [45] M. Yang, Y. Lv, J. Wang, C. Ding, J. Wang, L. Ma, K. Zhang, P. Liu, *Int. J. Hydrog. Energy* 47 (2022) 27023–27031.
- [46] A. Dauscher, L. Hilaire, F. Le Normand, W. Müller, G. Maire, A. Vasquez, *Surf. Interface Anal.* 16 (1990) 341–346.
- [47] A.F. Rigosi, H.M. Hill, N.R. Glavin, S.J. Pookpanratana, Y. Yang, A.G. Boosalis, J. Hu, A. Rice, A.A. Allerman, N.V. Nguyen, C.A. Hacker, R.E. Elmquist, A.R. Hight Walker, D.B. Newell, *2D Mater.* 5 (2017), 011011.
- [48] D. Gogoi, R.S. Karmur, M.R. Das, N.N. Ghosh, *Appl. Catal. B: Environ.* 312 (2022), 121407.
- [49] X. Zeng, H. Chen, X. He, H. Zhang, W. Fang, X. Du, W. Li, Z. Huang, L. Zhao, *Environ. Res.* 207 (2022), 112178.
- [50] J. Fan, Y. Zhao, H. Du, L. Zheng, M. Gao, D. Li, J. Feng, *ACS Appl. Mater. Interfaces* 14 (2022) 26752–26765.
- [51] L. Jiang, Y. Li, X. Wu, G. Zhang, *Sci. China Mater.* 64 (2021) 2230–2241.
- [52] R. Pang, S. Wang, *Nanoscale* 14 (2022) 3416–3424.
- [53] J. Sung, Y. Zhou, G. Scuri, V. Zolyomi, T.I. Andersen, H. Yoo, D.S. Wild, A.Y. Joe, R. J. Gelly, H. Heo, S.J. Magorrian, D. Bérubé, A.M.M. Valdivia, T. Taniguchi, K. Watanabe, M.D. Lukin, P. Kim, V.I. Fal'ko, H. Park, *Nat. Nanotechnol.* 15 (2020) 750–754.
- [54] V.I. Gol'danskiĭ, V.V. Kuz'min, *Sov. Phys. Usp.* 32 (1989) 1–29.
- [55] K.M. Kamal, R. Narayan, N. Chandran, S. Popovic, M.A. Nazrulla, J. Kovač, N. Vrtovec, M. Bele, N. Hodnik, M.M. Kržmanc, B. Likozar, *Appl. Catal. B: Environ.* 307 (2022), 121181.
- [56] Y. Shi, G. Zhan, H. Li, X. Wang, X. Liu, L. Shi, K. Wei, C. Ling, Z. Li, H. Wang, C. Mao, X. Liu, L. Zhang, *Adv. Mater.* 33 (2021), 2100143.